Ion-Induced Surface Charge Dynamics in Freestanding Monolayers of Graphene and MoS₂ Probed by the Emission of Electrons

Anna Niggas[1,*] Janine Schwestka[1] Karsten Balzer,[2,†] David Weichselbaum,[1] Niclas Schlünzen,[3,‡] René Heller,[4] Sascha Creutzburg[4] Heena Inani[5] Mukesh Tripathi[5] Carsten Speckmann[5,6] Niall McEvoy[7] Toma Susi[5] Jani Kotakoski[5] Ziyang Gan[8] Antony George[8] Andrey Turchanin[8] Michael Bonitz,[3,9] Friedrich Aumayr[1] and Richard A. Wilhelm[1,§]

[1]TU Wien, Institute of Applied Physics, 1040 Vienna, Austria
[2]Computing Center of Kiel University, 24118 Kiel, Germany
[3]Kiel University, Institute for Theoretical Physics and Astrophysics, 24098 Kiel, Germany
[4]Helmholtz-Zentrum Dresden-Rossendorf, Institute of Ion Beam Physics and Materials Research, 01328 Dresden, Germany
[5]University of Vienna, Faculty of Physics, 1090 Vienna, Austria
[6]University of Vienna, Vienna Doctoral School in Physics, 1090 Vienna, Austria
[7]Trinity College Dublin, Advanced Materials and Bioengineering Research Centre (AMBER) and School of Chemistry, College Green, Dublin 2, Ireland
[8]Friedrich Schiller University Jena, Institute of Physical Chemistry, 07743 Jena, Germany
[9]Kiel Nano, Surface and Interface Science KiNSIS, Kiel, Germany

We compare the ion-induced electron emission from freestanding monolayers of graphene and MoS₂ to find a sixfold higher number of emitted electrons for graphene even though both materials have similar work functions. An effective single-band Hubbard model explains this finding by a charge-up in MoS₂ that prevents low energy electrons from escaping the surface within a period of a few femtoseconds after ion impact. We support these results by measuring the electron energy distribution for correlated pairs of electrons and transmitted ions. The majority of emitted primary electrons have an energy below 10 eV and are therefore subject to the dynamic charge-up effects at surfaces.

The dynamics of an ion impact on a solid surface is governed by a plethora of processes from the sub-fs to the ns range. While the ion impact and associated electronic processes like charge exchange and (electronic) stopping can be probed by ion transmission spectroscopy [1,2], the electronic and nuclear dynamics in the material after the ion has passed the surface stay hidden from direct experimental observation. The ion-induced dynamics in a material, however, are the driving force for all material modifications used in surface science and industrial applications of ion beams. Electronic excitations are well comparable to (if not even larger than) the effects of intense short-laser pulses at surfaces (except for resonant processes), but acting on the nanoscale only [3–6]. The observation and analysis of emitted particles offers an experimental access to ion-related processes, since they may either originate from delayed secondary processes or their emission characteristics are influenced by the dynamic material response to the ion impact. From the early days of solid state physics, the emission of electrons was characterized by the material's work function, i.e., the constant energy for the emission of a single electron within the effective potential formed by all other (bound) electrons. While this allows for a description of small excitations, the rationality of this model needs to be discussed for the case of many emitted particles in one instance with an additional excitation introduced by the ion. Here, we show—in the time and space domain—that the description of a static single-electron work function is not applicable for a highly excited surface.

Electron emission from metals, semiconductors, and insulators induced by heavy ion impact was investigated for several bulk materials in the past [7–17]. Differences in the number of emitted electrons depending on the electronic band structure of the investigated solid were observed, but were difficult to describe as the electrons' mean free path varies for insulators and metals at low electron energies [18,19]. At that time these observations were interpreted as a result of varying above and below surface contributions to the electron emission yield. Auger electron emission induced by heavy ion impact on bulk LiF and LiF coated Au(110) [20] were compared, as well as from metallic Be and insulating BeO surfaces [21]. In both studies, the similarities in the observed spectra suggested a vanishing influence of the band gap or even a breakdown of the band structure once strong electronic excitations are introduced in the surface. Here we make use of freestanding 2D membranes as solid targets and directly address the

response of a pure surface to an ion impact by excluding both electron attenuation and multiplication contributions to the total number of emitted electrons along the electron inelastic mean free path. We directly detect the primary electrons emitted from the ion-surface interaction process similar to data obtained from ion-molecule scattering in reaction microscopes [22–27]. In contrast, earlier literature was mostly limited to secondary (and higher order) electrons from electron cascades in ion-surface collisions [8–10]. We follow the evolution of free electrons created within a surface, starting from their release in an emission process followed by escape from the 2D layer. We show that the number and energy distribution of electrons in an experiment is a direct measure for their escape probability under the influence of ion-induced surface charge dynamics which may [molybdenum disulfide (MoS_2) [28]] or may not (graphene [29]) trigger electronic sputtering and perforation of 2D layers.

We irradiate freestanding 2D monolayers of graphene and MoS_2 with highly charged ions (HCIs) of xenon at charge states ranging from 20 to 40, i.e., initial potential energies of 4.5 to 38.5 keV. Ion velocities $v \ll v_0$ (Bohr velocity: $v_0 = 2.19 \times 10^6$ m/s) are chosen to initiate charge exchange already above the surface [30]. An electron beam ion source (Dreebit EBIS-A [31,32]) is used to provide the high charge states. By means of a Wien filter we then select certain charge states and adjust their kinetic energy by applying a negative potential to the ion source. The number of ejected electrons is measured along with the corresponding transmitted ion with a coincidence technique, described in more detail in [33,34]. Alternatively, the electrons are detected in a SPECS EA10+ hemispherical energy analyzer (HEA), again in coincidence with the transmitted ions. Both electron detectors are mounted perpendicular to the incoming ion beam [see Fig. 1(a)]. Samples are mounted on TEM grids with Quantifoil (QF) support. Graphene samples are commercially obtained from Graphenea. MoS_2 samples are grown by CVD on SiO_2 in Jena [35,36] and Dublin [37] and transferred onto TEM grids by standard methods [38]. Samples are heated to $\sim 400\,°C$ prior to the measurement under UHV conditions for several hours and kept at $\sim 200\,°C$ during the measurement to avoid recontamination. The cleaning method and data acquisition are described in [39]. The electron statistics detector used to determine the yield of emitted electrons is described in [7,40]. In short, we use a positively biased grid to collect the emitted electrons and a high voltage (~ 30 kV) biased silicon surface barrier (PIPS) detector behind the grid. The detector output signal is proportional to the amount of deposited energy of all electrons emitted by a single ion, i.e., $n \times 30$ keV, if n is the number of emitted electrons. Using a Roentdek CFD1x constant fraction discriminator and a TDC8HP time-to-digital converter allows us to evaluate the electron emission yield encoded in the length of a timing pulse
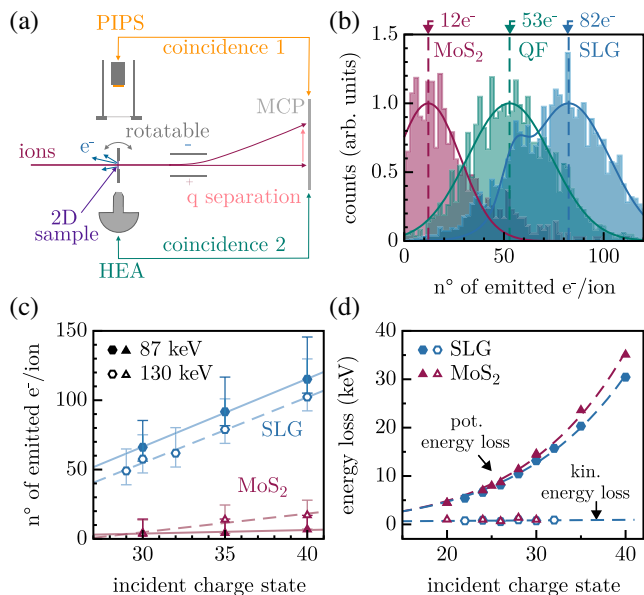

FIG. 1. (a) Schematic of the experimental setup including an electron statistics (PIPS) detector, an HEA as well as a pair of deflection plates for charge state separation on the DLD. (b) Electron emission spectra for 130 keV Xe^{35+} ions transmitted through MoS_2, SLG, and the targets' QF support. (c) Mean number of emitted electrons from MoS_2 and SLG for 87 and 130 keV Xe ions. (d) Potential and kinetic energy loss of 130 keV Xe ions in MoS_2 and SLG. Lines are shown to guide the eye.

together with the overall timing information, i.e., in coincidence with the (charge separated) ions detected after transmission on a delay line detector (DLD) [41]. In addition to the results obtained at the electron statistics detector we also perform coincidence measurements with a HEA to determine the energy distribution of emitted electrons. The ion impact angle on the sample is adjusted to about $\pm 30°$ with respect to the incoming ion beam for electron statistics and $\pm 40°$ for electron energy measurements, respectively, in order to increase the electron collection efficiency.

Electron emission distributions are shown in Fig. 1(b) as an example for MoS_2, QF, and single layer graphene (SLG). Each spectrum can be fitted by a Gaussian [7,40] whose mean value is the average number of emitted electrons due to a single ion impact. The electron emission yield from the QF support used in both SLG and MoS_2 samples can be used as a reference to guarantee the same detection efficiency for both samples and thus allowing the direct comparison in the number of emitted electrons under identical experimental conditions. To distinguish between electron emission induced by ion impact on the sample, its QF support and the TEM grid itself, the ion's time-of-flight (TOF) is recorded using the electron signal as a start trigger and the ion impact on the DLD as a stop trigger. All data are stored in a list mode file and can be filtered for different TOF conditions after measurement. In SLG, the TOF distribution of the ions does not always separate well

enough from the one of ions passing QF, which leads to a shoulder at lower yields in the determined electron emission yield shown in Fig. 1(b) after data filtering. The same TOF filtering is applied for the HEA measurements. Electron emission yields for ions in different charge states and two different kinetic energies from the two materials are shown in Fig. 1(c). We observe a total electron yield for SLG on average about six times higher than for MoS_2 under the same ion irradiation conditions. This factor and the total number of emitted electrons seem to be almost independent of the ion's kinetic energy, as we reported earlier for SLG [42]. The yield increases with increasing ion charge state for both materials, pointing clearly towards an emission process triggered by the ion's potential energy deposition. The kinetic emission yield from graphite under the same conditions is about 2–3 [43,44]. Large amounts of emitted electrons were observed in the past after bombarding insulating surfaces such as LiF(001) and $CaF_2(111)$ with highly charged Xe ions [11,45]. For LiF(001), the number of measured electrons even exceeds the one observed from a clean Au(111) surface despite the considerably lower work function of the metal. A delayed charge capture in front of the insulating surface and a larger mean free path in insulators in general were concluded as the origin for additionally created subsurface secondary electrons contributing to the total measured yield. For each electron emission event, the potential energy deposition determined by the difference in incoming and on-average outgoing charge states is in fair agreement for both materials [cf. Fig. 1(d)]. The slightly higher value for MoS_2 (about 10%) can be attributed to the increased transmission time through the triple-atomic-layer structure [46]. The difference in the ion's kinetic energy loss is negligibly small [100–200 eV, cf. Fig. 1(d)]. Hence, the energy deposition via HCI irradiation is dominated by the potential energy. Furthermore, we can conclude that the majority of the ion's initial potential energy, 85% in case of SLG and 95% in MoS_2, is released within the material. In the case of 130 keV Xe^{35+}, this means energies of 20.3 and 23.6 keV are transferred into the target electronic system for both materials, respectively. There remains a main difference in the conversion of this excitation energy for both 2D materials which is reflected in the electron emission yield. As we observe projectile neutralization within femtoseconds in both materials [29,46,47], we further expect strong electronic excitations of same magnitude in both targets. Still, we observe a strong difference in the measured electron emission yield. The work function, which mainly influences the energy required for ionization, is comparable for both materials, about 4.6 eV for graphene [48,49] and 4.5 eV for MoS_2 [50,51].

It is commonly known that electronic excitations accommodate in metals more quickly (10^{-14} s) than in semiconductors (10^{-13} to 10^{-12} s) [52]. As a consequence, local charge buildups in insulators and semiconductors may dissipate on a longer timescale, which even later (10^{-12} to 10^{-11} s) might lead to surface modifications such as hillocks and pits [53–55] or even material rupture of foils [45,56]. Especially for suspended monolayer semiconductors this charge-up can become severe as electrons cannot be resupplied from layers below [28].

Let us review the origin of the electron emission. At a certain distance toward its way to the surface, the ion starts to capture electrons resonantly into high-lying n shells and, as a consequence, a hollow atom (HA) with empty inner and intermediate electron shells forms [30]. Upon target impact, the HA collapses rapidly via an interatomic Auger deexcitation, the interatomic Coulombic decay (ICD)—a process also recently observed in liquid water [57]—and thereby transfers its excitation energy into the electronic system of the monolayer [58].

To study the charge dynamics in the surface further, we performed calculations based on a HCI-surface interaction model [59], where both target materials are described in terms of an effective single-band Hubbard model for a finite, hexagonal 2D honeycomb lattice with a lattice constant of 2.46 Å (3.17 Å) for SLG (MoS_2) and 216 sites. The Hamiltonian has the general form $\hat{H} = \hat{H}_0 + \hat{H}_1$, where $\hat{H}_0 = \hat{E} + \hat{J} + \hat{U}$ incorporates the on-site energy $\hat{E} = E \sum_{i\sigma} \hat{c}_{i\sigma}^\dagger \hat{c}_{i\sigma}$, the tunneling of electrons between nearest neighbor sites $\hat{J} = -J \sum_{\langle i,j \rangle \sigma} \hat{c}_{i\sigma}^\dagger \hat{c}_{j\sigma}$, and a local Coulomb repulsion $\hat{U} = U \sum_i (\hat{n}_{i\uparrow} - 1/2)(\hat{n}_{i\downarrow} - 1/2)$, which is treated in Hartree approximation. Furthermore, $\hat{H}_1 = \hat{V} + \hat{W}_x$ describes the interaction with the ion, where $\hat{V} = \sum_{i\sigma} V_i[S(t)]\hat{c}_{i\sigma}^\dagger \hat{c}_{i\sigma}$ denotes the ion-induced potential energy for a normal incidence, central impact ion trajectory $S(t)$ with fixed velocity and charge state, and $\hat{W}_x = \sum_{k\sigma} \gamma_k[S(t)][\hat{a}_{k\sigma}^\dagger(\epsilon)\hat{c}_{k\sigma} + \text{H.c.}]$ accounts for resonant charge transfer from sites k of the central honeycomb into an effective high lying n shell of the ion with energy ϵ. Initially the Hubbard system is half-filled (0.5 electrons per site and spin σ), and assuming the occupation of four equal, noninteracting bands gives access to the simulation of four active valence electrons per site. We compute the time evolution of the local electron density, $\langle \hat{n}_{i\sigma} \rangle(t) = \langle \hat{c}_{i\sigma}^\dagger \hat{c}_{i\sigma} \rangle(t)$, during the charge exchange with the HCI, using the method of nonequilibrium Green functions [60–62] combined with an Ehrenfest approach for the ion [3,4] and an embedding self-energy approach for the charge transfer [59,63]. Differences in electron mobility and conductivity of both materials enter via the nearest-neighbor hopping J and the Hubbard interaction strength U, respectively, and minimal differences in the work function are considered in the on-site energy E. The model parameters are $J = 2.8$ eV (1.1 eV), $U/J = 1.6$ (4.0) and $E = -4.6$ eV (-4.5 eV) for SLG (MoS_2) [48–51], and the tunneling amplitude $\gamma_k(t)$ and energy ϵ are chosen as in [59].

While the generation of free electrons is not explicitly included in the model, the spatiotemporal resolution of the
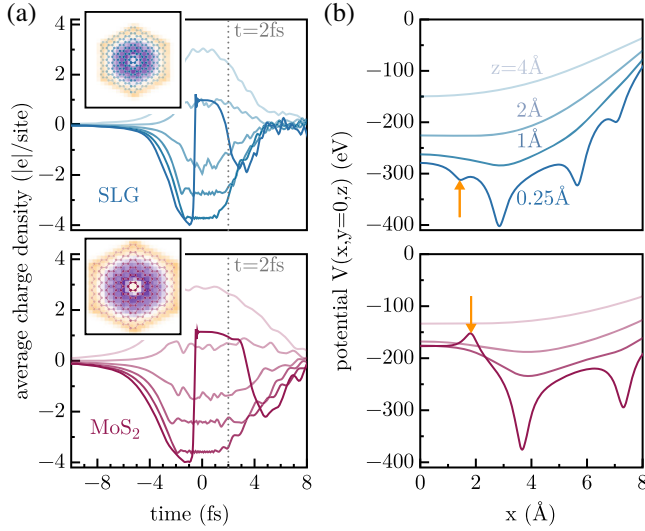
FIG. 2. HCI-monolayer interaction for 113 keV Xe^{32+} centrally passing through SLG (top, blue) and MoS$_2$ (bottom, violet). (a) Ion-induced change of local charge neutrality in the target, obtained from the model's electron density averaged over equally colored lattice sites (cf. inset). (b) Electrostatic potential, $V(\mathbf{r}, t)$, induced by the target's charge density at $t = 2$ fs, versus radial coordinate x, at four distances z from the monolayer. The arrows indicate the position of the innermost honeycomb from which electron emission is expected to occur primarily.

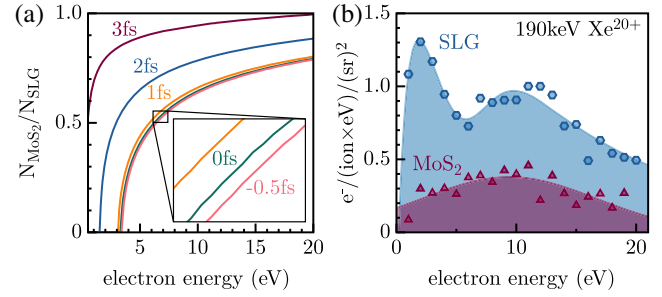

FIG. 3. (a) Computed detection ratio of electrons emitted from SLG and MoS$_2$ as a function of their initial kinetic energy at a distance of 0.8 Å from the monolayer, following from a classical trajectory analysis using the time-dependent potential presented in Fig. 2. The time stamps define the emission time of the electrons (cf. Fig. 2). (b) Experimentally determined electron energy distribution of SLG and MoS$_2$ induced by 190 keV Xe^{20+} ion impacts.

electron density $\langle \hat{n}_{i\sigma} \rangle(t)$ allows us to draw conclusions about their emission probability at certain points in time. In fact, the deviation from local charge neutrality $\Delta \rho_i(t) = 4|e|(1 - \sum_\sigma \langle \hat{n}_{i\sigma} \rangle(t))$ at site coordinate $\mathbf{r}_i$ gives rise to a time-dependent induced potential landscape, $V(\mathbf{r}, t) = (4\pi\epsilon_0)^{-1} \sum_i \Delta \rho_i(t)/|\mathbf{r} - \mathbf{r}_i|$. Whether an electron, which is created with a specific kinetic energy at point $\mathbf{r}$, will leave the system and contribute to the electron yield or will be recaptured, is governed by the local force, $|e| \cdot \nabla V(\mathbf{r}, t)$ and, thus, by the local charge-up.

Figure 2(a) shows the ion-induced change of local charge neutrality in both targets for 113 keV Xe^{32+}, averaged over lattice sites that belong to the same hexagon shell of the lattice (innermost hexagon: dark, outermost hexagon: light; cf. equally colored lattice sites in the insets). While the ion generally attracts electrons toward the lattice center and thus depletes the edge states, the decline of $\langle \hat{n}_{i\sigma} \rangle$ (increase of $\Delta \rho_i$) on the central honeycomb before the ion impact (at $t = 0$) is due to resonant electron transfer to the ion. The simulation result for the final charge state of the ion is approximately $q_{\text{out}} = 9$, for SLG, and $q_{\text{out}} = 1$, for MoS$_2$. Insets show the charge density profile at $t = 2$ fs (violet: negative, orange: positive charge). Figure 2(b) shows the electrostatic potential $V(x, y = 0, z, t = 2 \text{ fs})$ for $z = 0.25$, 1, 2, and 4 Å. Here, we observe a clear difference in the potentials for SLG and MoS$_2$ as electrons are accelerated for SLG and decelerated for MoS$_2$ (i.e., more negative potential at $z = 1$ than 0.25 Å) when being emitted from the central lattice sites (orange arrows). To compare to the

measured electron emission yield we performed a classical trajectory analysis, similar to that in Refs. [64,65], using the time-dependent potential following from Fig. 2. In Fig. 3(a) we present the computed ratio of electrons emitted from graphene and MoS$_2$, versus initial kinetic energy, and five emission times. Please note, that for graphene all electrons are able to leave the sample at all times and the ratio is primarily determined by emission from MoS$_2$. For high electron energies and/or late emission times we find that the ratio of detected electrons converges to 1, i.e., for both samples all emitted electrons reach the detector. To reconcile this with our experiment we measured the energy distribution of electrons emitted from SLG and MoS$_2$. All data points result from correlated electron-ion pairs linked via the ion TOF. Figure 3(b) shows a comparison of the measured electron energy distributions of SLG and MoS$_2$, where we find that mean energies for both materials are $\sim$10 eV. This coincides well with the energy range in Fig. 3(a), where a large difference in detection efficiency for electrons starting within < 2 fs after ion impact from the two materials is expected [see Fig. 3(a) and the Appendix for a more quantitative comparison, respectively]. This effect might also explain a distortion of the MoS$_2$ energy distribution in comparison to SLG, e.g., variations at energies < 10 eV. A detailed discussion of the structure of the electron spectra is, however, beyond the scope of this Letter. Additional noncoincidence measurements show that there is no sizable contribution of electrons with energies above 20 up to 200 eV. Please note that the transmission of the HEA may decrease for very small energies and we cannot exclude the presence of small residual magnetic stray fields. We conclude that a local, highly dynamic charge-up is the major reason for the reduction in the electron emission yield from MoS$_2$ as this prevents slow electrons from leaving the positively charged surface and/or triggers electron recapture toward the ion's impact point after emission. The charging can, therefore, be

interpreted as an effective transient increase of the work function of MoS_2, hindering low energy electrons from escaping the surface. For graphene, a similarly strong charge-up is seen, which, however, decays much faster. Charge carrier mobilities in graphene, in general, are about 1000 times higher than in semiconducting 2D MoS_2 [66]. Our model used to describe these ultrafast charge carrier dynamics is universal and can in general be adapted to any lattice. From our Letter we can conclude that the ion-induced electron emission at a surface is prompt, i.e., starts within the first femtoseconds after the ion impact. It is subject to a complex manybody problem and renders the application of the conventional material work function doubtful. The ion induces a highly nonequilibrium and nonuniform state very different from all traditional investigations, including the rates for resonant charge transfer, Auger ionization or ICD, which are typically derived for systems in or close to the ground state. The approaching ion creates a completely new physical situation that cannot be created by other types of excitation. Complementary calculations of the ion induced change of the electron energy spectrum in the two materials are shown in the Appendix. The present experiment provides not only an ultrafast diagnostic of the ion, but also a unique diagnostic of the surface with single site resolution. Delayed electron emission from, for example, a plasmon decay [67–71] may play only a minor role and an extended electron collision cascade is suppressed in 2D materials. Even though the temporal evolution of the introduced surface charge shows only small differences ($\sim$2 fs) in whether a semimetallic or semiconducting surface is probed, the electron emission is very sensitive to it. The observation of emitted electrons serves therefore as a probe for dynamic effects on the femtosecond timescale, which offers the possibility to study highly nonequilibrium ion-induced electronic processes on the nanoscale where no direct time resolution is currently possible. Our approach bridges the gap from time-resolved ultrafast laser spectroscopy to ion physics and helps to understand exotic electronic excitations at surfaces in general.

Appendix: Additional simulation results—To gain a more quantitative comparison between our experiment and model data, we performed additional molecular dynamics simulations. The data shown in Fig. 3(a) build upon a fixed starting value $z = 0.8$ Å above the surface for emitted electrons. For Fig. 4(a), we used probability distributions for electrons in various orbitals (of graphene) and a charge density obtained from scanning tunneling microscopy measurements [72]. Since ion de-excitation via ICD and/or Auger processes happen on the (sub-)femtosecond timescale [58], we chose the potentials for $t = 0$ [Fig. 2(b)] for the simulation results presented in Fig. 4(a). Especially for the charge density from STM measurements (red) the computed MoS_2/graphene electron detection ratio spectrum agrees well with experimentally found data (black dots). This connection of electron energy and emission probability, in general, allows for an analysis of emission times, which opens a new field to studying material response due to ion interaction. From the results presented in our manuscript we can deduce that electron emission is prompt and happens within the first 1–3 fs after the ion impact.

To examine the electron energy spectrum prior to the emission period, we performed further calculations using nonequilibrium Green functions [3,4] within the G1–G2 scheme, where we included electronic
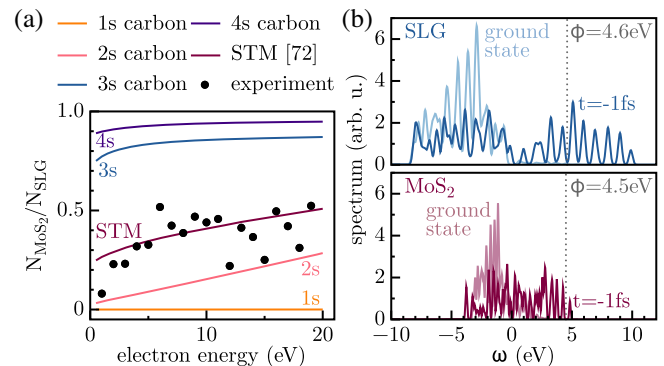
FIG. 4. (a) Molecular dynamics simulations for computation of the ratio of detected MoS_2/graphene electrons in dependence of the electron energy using the potentials shown in Fig. 2(b) for $t = 0$. The emission origin stems from averaging probability distributions for various orbitals and a charge density obtained from STM measurements [72], respectively. Experimental data points are added in black circles. (b) Energy spectrum of graphene and MoS_2 for the ground state and $t = -1$ fs before the impact of a 113 keV Xe^{32+} ion. The latter is a highly nonequilibrium state from which complex charge transfer processes and electron emission start. Vertical lines indicate the work functions ϕ of the respective materials. G1–G2 simulations with second order Born self-energies [5] for honeycomb targets containing 96 sites.

correlations in the target on the level of the second Born approximation [5,73,74]. This allows us to explore changes in the density of states due to the ion impact. So far, no resonant charge transfer is included in these simulations. In Fig. 4(b) we compare the energy spectra of graphene and MoS_2, both for the ground state and for $t = -1$ fs before the ion impact, which corresponds to the time when resonant charge transfer sets in, according to the results in Fig. 2(a). The spectra were computed using Koopmans theorem [75]. It is apparent that for graphene electrons are excited to significantly higher energies than for MoS_2, which is primarily due to the larger bandwith and higher carrier mobility of graphene, as compared to MoS_2. These out of equilibrium energy spectra are the starting point for the resonant charge transfer as well as ionization (or Auger) processes. They provide additional explanations for the striking differences in the measured electron emission spectra in the two materials. The extremely short duration of the ion-solid interaction gives rise to the excitation of many electronic transitions simultaneously, whereas the high ion charge promotes a substantial number of electrons into the upper band, as seen in Fig. 4(b). It is instructive to compare these spectra to photoemission spectra from graphene nanoribbons irradiated by a few-cycle laser pulse [6]. For moderate laser intensities (sufficiently well below the field ionization threshold) and away from resonant transitions the excitation of the electron system is significantly weaker than in the case of a highly charged ion presented above. On the other hand, by adjusting the photon energy to a certain energetic transition in the target, lasers one can selectively populate excited states via (multiple) photon absorption—a physical mechanism that is missing in the case of ion impact. Thus, an ion impact is complementary to laser excitation. Aside from the field strength and its time dependence, also the spatial dependence of the field strength is crucial for material diagnostics, as it determines the spatial resolution. Here, laser pulses are typically uniform over many nanometers (at least) whereas an ion impact is maximally localized. This gives rise to high field gradients and to strong in-plane transport of electrons which has been shown to be crucial for electron emission (graphene vs MoS_2) in the present Letter. Moreover, this high spatial resolution makes the direct measurement of electronic transport properties, such as mobility, diffusion, conductivity, etc., under extreme conditions accessible. These properties are strongly influenced by electronic correlation effects in quantum materials, and ion impact experiments pave the way for precise measurements and theory-experiment comparisons.

---

[*] niggas@iap.tuwien.ac.at

[†] balzer@rz.uni-kiel.de

[‡] Present address: Center for Advanced Systems Understanding (CASUS), Görlitz, 02826, Germany.

[§] wilhelm@iap.tuwien.ac.at

[1] R. A. Wilhelm, E. Gruber, R. Ritter, R. Heller, S. Facsko, and F. Aumayr, Charge Exchange and Energy Loss of Slow Highly Charged Ions in 1 nm Thick Carbon Nanomembranes, Phys. Rev. Lett. **112**, 153201 (2014).

[2] S. Lohmann and D. Primetzhofer, Disparate Energy Scaling of Trajectory-Dependent Electronic Excitations for Slow Protons and He Ions, Phys. Rev. Lett. **124**, 096601 (2020).

[3] K. Balzer, N. Schlünzen, and M. Bonitz, Stopping dynamics of ions passing through correlated honeycomb clusters, Phys. Rev. B **94**, 245118 (2016).

[4] K. Balzer, M. R. Rasmussen, N. Schlünzen, J.-P. Joost, and M. Bonitz, Doublon Formation by Ions Impacting a Strongly Correlated Finite Lattice System, Phys. Rev. Lett. **121**, 267602 (2018).

[5] N. Schlünzen, J.-P. Joost, and M. Bonitz, Achieving the Scaling Limit for Nonequilibrium Green Functions Simulations, Phys. Rev. Lett. **124**, 076601 (2020).

[6] J.-P. Joost, N. Schlünzen, and M. Bonitz, Femtosecond electron dynamics in graphene nanoribbons—A nonequilibrium Green functions approach within an extended Hubbard model, Phys. Status Solidi (b) **256**, 1800498 (2019).

[7] F. Aumayr, G. Lakits, and H. Winter, On the measurement of statistics for particle-induced electron emission from a clean metal surface, Appl. Surf. Sci. **47**, 139 (1991).

[8] F. Aumayr, H. Kurz, D. Schneider, M. A. Briere, J. W. McDonald, C. E. Cunningham, and H. P. Winter, Emission of Electrons from a Clean Gold Surface Induced by Slow, Very Highly Charged Ions at the Image Charge Acceleration Limit, Phys. Rev. Lett. **71**, 1943 (1993).

[9] H. Kurz, F. Aumayr, C. Lemell, K. Töglhofer, and H. P. Winter, Neutralization of slow multicharged ions at a clean gold surface: Electron-emission statistics, Phys. Rev. A **48**, 2192 (1993).

[10] M. Vana, F. Aumayr, C. Lemell, and H. P. Winter, Ion-induced electron emission from solid surfaces: Information content of the electron number statistics, Int. J. Mass Spectrom. Ion Process. **149–150**, 45 (1995).

[11] W. Meissl, D. Winklehner, F. Aumayr, M. C. Simon, R. Ginzel, J. R. C. López-Urrutia, J. Ullrich, B. Solleder, C. Lemell, and J. Burgdörfer, Electron emission from insulators irradiated by slow highly charged ions, e-J. Surf. Sci. Nanotechnol. **6**, 54 (2008).

[12] E. Bodewits, R. Hoekstra, G. Kowarik, K. Dobes, and F. Aumayr, Highly-charged-ion-induced electron emission from C_{60} thin films, Phys. Rev. A **84**, 042901 (2011).

[13] E. Bodewits, R. Hoekstra, K. Dobes, and F. Aumayr, Electron-emission processes in highly charged Ar and Xe ions impinging on highly ordered pyrolytic graphite at energies just above the kinetic threshold, Phys. Rev. A **90**, 052703 (2014).

[14] A. Phelps and Z. L. Petrovic, Cold-cathode discharges and breakdown in argon: Surface and gas phase production of secondary electrons, Plasma Sources Sci. Technol. **8**, R21 (1999).

[15] A. Derzsi, I. Korolov, E. Schüngel, Z. Donkó, and J. Schulze, Effects of fast atoms and energy-dependent secondary electron emission yields in PIC/MCC simulations of capacitively coupled plasmas, Plasma Sources Sci. Technol. **24**, 034002 (2015).

[16] M. Bonitz, A. Filinov, J.-W. Abraham, K. Balzer, H. Kählert, E. Pehlke, F. X. Bronold, M. Pamperin, M. Becker, D. Loffhagen *et al.*, Towards an integrated modeling of the plasma-solid interface, Front. Chem. Sci. Eng. **13**, 201 (2019).

[17] S. Lohmann, A. Niggas, V. Charnay, R. Holeňák, and D. Primetzhofer, Assessing electron emission induced by pulsed ion beams: A time-of-flight approach, Nucl. Instrum. Methods Phys. Res., Sect. B **479**, 217 (2020).

[18] D. Geelen, J. Jobst, E. E. Krasovskii, S. J. van der Molen, and R. M. Tromp, Nonuniversal Transverse Electron Mean Free Path through Few-Layer Graphene, Phys. Rev. Lett. **123**, 086802 (2019).

[19] W. S. M. Werner, Questioning a universal law for electron attenuation, Physics **12**, 93 (2019).

[20] H. Khemliche, T. Schlathölter, R. Hoekstra, R. Morgenstern, and S. Schippers, Hollow Atom Dynamics on LiF Covered Au(111): Role of the Surface Electronic Structure, Phys. Rev. Lett. **81**, 1219 (1998).

[21] G. Schiwietz, K. Czerski, M. Roth, P. L. Grande, V. Koteski, and F. Staufenbiel, Evidence for an Ultrafast Breakdown of the BeO Band Structure due to Swift Argon and Xenon Ions, Phys. Rev. Lett. **105**, 187603 (2010).

[22] R. Moshammer, M. Unverzagt, W. Schmitt, J. Ullrich, and H. Schmidt-Böcking, A 4π recoil-ion electron momentum analyzer: A high-resolution "microscope" for the investigation of the dynamics of atomic, molecular and nuclear reactions, Nucl. Instrum. Methods Phys. Res., Sect. B **108**, 425 (1996).

[23] J. Ullrich, R. Moshammer, A. Dorn, R. Dörner, L. P. H. Schmidt, and H. Schmidt-Böcking, Recoil-ion and electron momentum spectroscopy: Reaction-microscopes, Rep. Prog. Phys. **66**, 1463 (2003).

[24] F. Trinter, J. B. Williams, M. Weller, M. Waitz, M. Pitzer, J. Voigtsberger, C. Schober, G. Kastirke, C. Müller, C. Goihl *et al.*, Evolution of Interatomic Coulombic Decay in the Time Domain, Phys. Rev. Lett. **111**, 093401 (2013).

[25] T. Ouchi, K. Sakai, H. Fukuzawa, I. Higuchi, Ph. V. Demekhin, Y.-C. Chiang, S. D. Stoychev, A. I. Kuleff, T. Mazza, M. Schöffler *et al.*, Interatomic Coulombic decay following Ne 1s Auger decay in NeAr, Phys. Rev. A **83**, 053415 (2011).

[26] T. Jahnke, V. Mergel, O. Jagutzki, A. Czasch, K. Ullmann, R. Ali, V. Frohne, T. Weber, L. Schmidt, S. Eckart *et al.*, High-resolution momentum imaging—From stern's molecular beam method to the coltrims reaction microscope, in *Molecular Beams in Physics and Chemistry* (Springer, New York, 2021), pp. 375–441.

[27] A. Méry, A. N. Agnihotri, J. Douady, X. Fléchard, B. Gervais, S. Guillous, W. Iskandar, E. Jacquet, J. Matsumoto, J. Rangama *et al.*, Role of a Neighbor Ion in the Fragmentation Dynamics of Covalent Molecules, Phys. Rev. Lett. **118**, 233402 (2017).

[28] R. Kozubek, M. Tripathi, M. Ghorbani-Asl, S. Kretschmer, L. Madauß, E. Pollmann, M. O'Brien, N. McEvoy, U. Ludacka, T. Susi, G. S. Duesberg, R. A. Wilhelm, A. V. Krasheninnikov, J. Kotakoski, and M. Y. Schleberger, Perforating freestanding molybdenum disulfide monolayers with highly charged ions, J. Phys. Chem. Lett. **10**, 904 (2019).

[29] E. Gruber, R. A. Wilhelm, R. Petuya, V. Smejkal, R. Kozubek, A. Hierzenberger, B. C. Bayer, I. Aldazabal, A. K. Kazansky, F. Libisch, A. V. Krasheninnikov, M. Schleberger, S. Facsko, A. G. Borisov, A. Arnau, and F. Aumayr, Ultrafast electronic response of graphene to a strong localized electric field, Nat. Commun. **7**, 13948 (2016).

[30] J. Burgdörfer, P. Lerner, and F. W. Meyer, Above-surface neutralization of highly charged ions: The classical over-the-barrier model, Phys. Rev. A **44**, 5674 (1991).

[31] G. Zschornack, M. Kreller, V. P. Ovsyannikov, F. Grossman, U. Kentsch, M. Schmidt, F. Ullmann, and R. Heller, Compact electron beam ion sources/traps: Review and prospects (invited), Rev. Sci. Instrum. **79**, 02A703 (2008).

[32] M. Schmidt, H. Peng, G. Zschornack, and S. Sykora, A compact electron beam ion source with integrated Wien filter providing mass and charge state separated beams of highly charged ions, Rev. Sci. Instrum. **80**, 063301 (2009).

[33] J. Schwestka, D. Melinc, R. Heller, A. Niggas, L. Leonhartsberger, H. Winter, S. Facsko, F. Aumayr, and R. A. Wilhelm, A versatile ion beam spectrometer for studies of ion interaction with 2D materials, Rev. Sci. Instrum. **89**, 085101 (2018).

[34] A. Niggas, J. Schwestka, D. Weichselbaum, R. Heller, F. Aumayr, and R. A. Wilhelm, Coincidence technique to study ion-induced electron emission from atomically thin materials, Proc. SPIE Int. Soc. Opt. Eng. **12131**, 121310H (2022).

[35] A. George, C. Neumann, D. Kaiser, R. Mupparapu, T. Lehnert, U. Hübner, Z. Tang, A. Winter, U. Kaiser, I. Staude, and A. Turchanin, Controlled growth of transition metal dichalcogenide monolayers using Knudsen-type effusion cells for the precursors, J. Phys. Mater. **2**, 016001 (2019).

[36] S. Shree, A. George, T. Lehnert, C. Neumann, M. Benelajla, C. Robert, X. Marie, K. Watanabe, T. Taniguchi, U. Kaiser *et al.*, High optical quality of MoS_2 monolayers grown by chemical vapor deposition, 2D Mater. **7**, 015011 (2019).

[37] M. O'Brien, N. McEvoy, T. Hallam, H.-Y. Kim, N. C. Berner, D. Hanlon, K. Lee, J. N. Coleman, and G. S. Duesberg, Transition metal dichalcogenide growth via close proximity precursor supply, Sci. Rep. **4**, 7374 (2015).

[38] J. C. Meyer, A. K. Geim, M. I. Katsnelson, K. S. Novoselov, T. J. Booth, and S. Roth, The structure of suspended graphene sheets, Nature (London) **446**, 60 (2007).

[39] A. Niggas, J. Schwestka, S. Creutzburg, T. Gupta, D. Eder, B. C. Bayer, F. Aumayr, and R. A. Wilhelm, The role of contaminations in ion beam spectroscopy with freestanding 2d materials: A study on thermal treatment, J. Chem. Phys. **153**, 014702 (2020).

[40] G. Lakits, F. Aumayr, and H. Winter, Statistics of ion induced electron emission from a clean metal surface, Rev. Sci. Instrum. **60**, 3151 (1989).

[41] U. Spillmann, O. Jagutzki, L. Spielberger, R. Dorner, V. Mergel, K. Ullmann-Pfleger, and H. Schmidt-Bocking, A novel design of delay-line anode for position and time sensitive read-out of MCP-based detectors, in *2000 IEEE Nuclear Science Symposium. Conference Record (Cat. No.00CH37149)* (IEEE, Lyon, France, 2000), Vol. 1, pp. 7/46–7/47.

[42] J. Schwestka, A. Niggas, S. Creutzburg, R. Kozubek, R. Heller, M. Schleberger, R. A. Wilhelm, and F. Aumayr, Charge-exchange-driven low-energy electron splash induced by heavy ion impact on condensed matter, J. Phys. Chem. Lett. **10**, 4805 (2019).

[43] D. Hasselkamp and A. Scharmann, Ion-induced electron emission from carbon, Phys. Status Solidi A **79**, K197 (1983).

[44] S. Cernusca, Electron emission and nanodefects due to slow ion impact on solid surfaces, Ph.D. thesis, TU Wien, 2003.

[45] R. A. Wilhelm, A. S. El-Said, F. Krok, R. Heller, E. Gruber, F. Aumayr, and S. Facsko, Highly charged ion induced nanostructures at surfaces by strong electronic excitations, Prog. Surf. Sci. **90**, 377 (2015).

[46] S. Creutzburg, J. Schwestka, A. Niggas, H. Inani, M. Tripathi, A. George, R. Heller, R. Kozubek, L. Madauß, S. Facsko, J. Kotakoski, M. Schleberger, A. Turchanin, P. L. Grande, F. Aumay, and R. A. Wilhelm, Vanishing influence of the band gap on charge exchange of slow highly charged ions in freestanding single layer MoS_2, Phys. Rev. B **102**, 045408 (2020).

[47] A. Niggas, S. Creutzburg, J. Schwestka, B. Wöckinger, T. Gupta, P. L. Grande, D. Eder, J. P. Marques, B. C. Bayer, F. Aumayr *et al.*, Peeling graphite layer by layer reveals the charge exchange dynamics of ions inside a solid, Commun. Phys. **4**, 180 (2021).

[48] Y.-J. Yu, Y. Zhao, S. Ryu, L. E. Brus, K. S. Kim, and P. Kim, Tuning the graphene work function by electric field effect, Nano Lett. **9**, 3430 (2009).

[49] M. Schüler, M. Rösner, T. O. Wehling, A. I. Lichtenstein, and M. I. Katsnelson, Optimal Hubbard Models for Materials with Nonlocal Coulomb Interactions: Graphene, Silicene, and Benzene, Phys. Rev. Lett. **111**, 036601 (2013).

[50] J. Shakya, S. Kumar, D. Kanjilal, and T. Mohanty, Work function modulation of molybdenum disulfide nanosheets by introducing systematic lattice strain, Sci. Rep. **7**, 9576 (2017).

[51] W. F. da Cunha, P. H. d. O. Neto, L. A. Ribeiro Junior, and G. M. e. Silva, Quasiparticle description of transition metal dichalcogenide nanoribbons, Phys. Rev. B **99**, 035405 (2019).

[52] B. Gonzalez, V. Palankovski, H. Kosina, A. Hernandez, and S. Selberherr, An energy relaxation time model for device simulation, Solid-State Electron. **43**, 1791 (1999).

[53] F. Aumayr, A. S. El-Said, and W. Meissl, Nano-sized surface modifications induced by the impact of slow highly charged ions—A first review, Nucl. Instrum. Methods Phys. Res., Sect. B **266**, 2729 (2008).

[54] A. S. El-Said, W. Meissl, M. C. Simon, J. R. C. López-Urrutia, I. C. Gebeshuber, M. Lang, H. P. Winter, J. Ullrich, and F. Aumayr, Surface nanostructures induced by slow highly charged ions on CaF_2 single crystals, Nucl. Instrum. Methods Phys. Res., Sect. B **256**, 346 (2007).

[55] A. S. El-Said, R. Heller, F. Aumayr, and S. Facsko, Pyramidal pits created by single highly charged ions in BaF_2 single crystals, Phys. Rev. B **82**, 033403 (2010).

[56] R. Ritter, R. A. Wilhelm, M. Stöger-Pollach, R. Heller, A. Mücklich, U. Werner, H. Vieker, A. Beyer, S. Facsko, A. Gölzhäuser, and F. Aumayr, Fabrication of nanopores in 1 nm thick carbon nanomembranes with slow highly charged ions, Appl. Phys. Lett. **102**, 063112 (2013).

[57] P. Zhang, C. Perry, T. T. Luu, D. Matselyukh, and H. J. Wörner, Intermolecular Coulombic Decay in Liquid Water, Phys. Rev. Lett. **128**, 133001 (2022).

[58] R. A. Wilhelm, E. Gruber, J. Schwestka, R. Kozubek, T. I. Madeira, J. P. Marques, J. Kobus, A. V. Krasheninnikov, M. Schleberger, and F. Aumayr, Interatomic Coulombic Decay: The Mechanism for Rapid Deexcitation of Hollow Atoms, Phys. Rev. Lett. **119**, 103401 (2017).

[59] K. Balzer and M. Bonitz, Neutralization dynamics of slow highly charged ions passing through graphene nanoflakes: An embedding self-energy approach, Contrib. Plasma Phys. **62**, e202100041 (2021).

[60] L. Kadanoff and G. Baym, *Quantum Statistical Mechanics* (Benjamin, New York, 1962).

[61] G. Stefanucci and R. van Leeuwen, *Nonequilibrium Many-Body Theory of Quantum Systems* (Cambridge University Press, Cambridge, England, 2013).

[62] K. Balzer and M. Bonitz, *Nonequilibrium Green's Functions Approach to Inhomogeneous Systems* (Springer, Berlin Heidelberg, 2013).

[63] N. Schlünzen, K. Balzer, M. Bonitz, L. Deuchler, and E. Pehlke, Time-dependent simulation of ion stopping: Charge transfer and electronic excitations, Contrib. Plasma Phys. **59**, e201800184 (2019).

[64] B. Schütte, S. Bauch, U. Frühling, M. Wieland, M. Gensch, E. Plönjes, T. Gaumnitz, A. Azima, M. Bonitz, and M. Drescher, Evidence for Chirped Auger-Electron Emission, Phys. Rev. Lett. **108**, 253003 (2012).

[65] S. Bauch and M. Bonitz, Theoretical description of field-assisted postcollision interaction in Auger decay of atoms, Phys. Rev. A **85**, 053416 (2012).

[66] J. Xue, S. Huang, J.-Y. Wang, and H. Q. Xu, Mott variable-range hopping transport in a MoS_2 nanoflake, RSC Adv. **9**, 17885 (2019).

[67] H. Felipe, L. Xian, A. Rubio, and S. G. Louie, Universal slow plasmons and giant field enhancement in atomically thin quasi-two-dimensional metals, Nat. Commun. **11**, 1013 (2020).

[68] G. Ni, d. A. McLeod, Z. Sun, L. Wang, L. Xiong, K. Post, S. Sunku, B.-Y. Jiang, J. Hone, C. R. Dean *et al.*, Fundamental limits to graphene plasmonics, Nature (London) **557**, 530 (2018).

[69] H. Yan, T. Low, W. Zhu, Y. Wu, M. Freitag, X. Li, F. Guinea, P. Avouris, and F. Xia, Damping pathways of mid-infrared plasmons in graphene nanostructures, Nat. Photonics **7**, 394 (2013).

[70] K. D. Chapkin, L. Bursi, G. J. Stec, A. Lauchner, N. J. Hogan, Y. Cui, P. Nordlander, and N. J. Halas, Lifetime dynamics of plasmons in the few-atom limit, Proc. Natl. Acad. Sci. U.S.A. **115**, 9134 (2018).

[71] A. Principi, G. Vignale, M. Carrega, and M. Polini, Intrinsic lifetime of dirac plasmons in graphene, Phys. Rev. B **88**, 195405 (2013).

[72] P. Xu, Y. Yang, S. Barber, M. L. Ackerman, J. K. Schoelz, I. A. Kornev, S. Barraza-Lopez, L. Bellaiche, and P. M. Thibado, Giant surface charge density of graphene resolved from scanning tunneling microscopy and first-principles theory, Phys. Rev. B **84**, 161409(R) (2011).

[73] J.-P. Joost, N. Schlünzen, and M. Bonitz, G1-G2 scheme: Dramatic acceleration of nonequilibrium Green functions

simulations within the Hartree-Fock generalized Kadanoff-Baym ansatz, Phys. Rev. B **101**, 245101 (2020).

[74] J.-P. Joost, N. Schlünzen, H. Ohldag, M. Bonitz, F. Lackner, and I. Březinová, Dynamically screened ladder approximation: Simultaneous treatment of strong electronic correlations and dynamical screening out of equilibrium, Phys. Rev. B **105**, 165155 (2022).

[75] T. Koopmans, Über die Zuordnung von Wellenfunktionen und Eigenwerten zu den Einzelnen Elektronen Eines Atoms, Physica **1**, 104 (1934).